

Contents lists available at ScienceDirect

# Colloids and Surfaces A: Physicochemical and Engineering Aspects

journal homepage: www.elsevier.com/locate/colsurfa



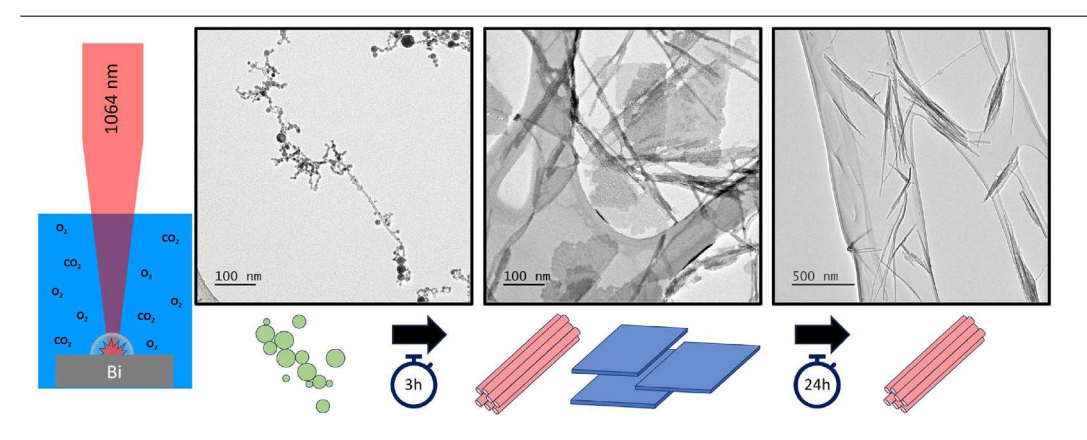


# Influence of environmental conditions on the morphological evolution of bismuth oxide nanostructures via pulsed laser ablation in liquids

Cory J. Trout a,b, Robert Albertson a, Julianne C. Griepenburg a,c, Sean M. O'Malley a,c,\*

- <sup>a</sup> Department of Physics, Rutgers University, 227 Penn Street, Camden, 08102, NJ, USA
- <sup>b</sup> Department of Applied Physics, Rutgers University, 101 Warren Street, Newark, 07102, NJ, USA
- <sup>c</sup> Center for Computational and Integrative Biology, Rutgers University, 201 Broadway, Camden, 08103, NJ, USA

#### GRAPHICAL ABSTRACT



# HIGHLIGHTS

- · Dissolved gases have an influence over the morphology of the bismuth nanostructures.
- · CO2 saturation results in the formation of bismuth oxide carbonate nanosheets.
- · At high fluences, the breakdown of water serves as an alternative source of oxygen.

#### ARTICLE INFO

Keywords:
Pulsed laser ablation
Bismuth oxide
Nanowires
Nanosheets
Morphological evolution
Colloidal aging

#### ABSTRACT

Bismuth oxide nanomaterials are increasingly recognized for their promising electronic and optical properties, particularly in electrochemical and biomedical applications. This study demonstrates that various bismuth oxide nanostructures can be synthesized through pulsed laser ablation in liquids (PLAL) by adjusting the concentration of dissolved gases from ambient conditions. Structural and compositional analyses were performed using x-ray diffraction, Raman spectroscopy, FTIR spectroscopy, and morphological investigations were conducted using atomic force microscopy and transmission electron microscopy. Our findings indicate that factors such as dissolved gases, laser fluence, and nanoparticle aging are crucial in determining the final structure and composition of the resulting nanomaterial. The phases observed ranged from spherical metallic bismuth nanoparticles to monoclinic bismuth oxide nanowire bundles, and orthorhombic bismuth carbonate oxide nanosheets. Dissolved gases are shown to influence not only the primary particles formed immediately after ablation, but also significantly impact the aging process of the colloid as well. Additionally,

<sup>\*</sup> Corresponding author at: Department of Physics, Rutgers University, 227 Penn Street, Camden, 08102, NJ, USA. E-mail address: omallese@camden.rutgers.edu (S.M. O'Malley).

fluence plays an important role in the production of reactive oxygen species, thereby influencing the reactive pathways experienced by the ablated material and its subsequent formation into nanostructures. A notable result, emphasizing the significance of factors such as liquid environment and fluence when performing PLAL on reactive targets like bismuth, is seen in high fluence (20 J/cm²) samples under ambient conditions. These samples initially display an amalgamation of  $\alpha$ -Bi<sub>2</sub>O<sub>3</sub> nanowire bundles and carbonate nanosheets, which upon aging, transition to predominantly bismuth oxide nanowire bundles. This contrasts with samples produced in a saturated CO<sub>2</sub> environment where bismuth carbonate nanosheets remain highly stable in the colloid.

#### 1. Introduction

Pulsed Laser Ablation in Liquids (PLAL) is a quasi-bottom-up technique for nanomaterial production, where a solid target submerged in liquid is irradiated with a pulsed laser. Upon irradiation, material from the solid target is ejected into the liquid solution providing the seed material for nanoparticle formation. The PLAL method has been widely used for various materials [1-9], with a significant focus on metallic targets such as gold and silver. The main interest in the method lies in its ability to control the size, concentration, and stability of the nanoparticle colloid [2,4,10,11]. Since these metals are relatively nonreactive, the potential to influence particle composition and structure is limited. Enhancing the tunability of the resulting nanomaterial produced by PLAL could be possible by selecting more reactive targets. This could allow for the production of nanomaterials with a composition different from the target, through interactions between the ejected target material and the surrounding solvent during and after ablation. Bismuth, in this context, makes for an interesting target material as its reactivity can be leveraged to control the composition, structure, and morphology of nanomaterials produced via PLAL.

The relatively high chemical reactivity of bismuth is owed to its electronic structure, where the outermost shell consists of a filled sorbital and 3-partially filled p-orbitals that have a high affinity to form covalent bonds. Bulk bismuth is classified as a semi-metal and assumes a rhombohedral lattice, that is both inexpensive and nontoxic. In addition, it displays unique optical and electronic properties when its dimensionality is restricted to the nanoscale [12-14]. For instance, a semimetal to semiconductor transition can be seen to occur due to quantum confinement effects forming a band gap [13]. Bismuth-based nanomaterials such as bismuth oxide and bismuth oxide carbonate demonstrate potential in biomedical, electrocatalytic, photocatalytic, and battery applications owing to their promising electronic and optical properties [15-17]. Various methods exist to produce bismuth-based nanomaterials, including thermal decomposition, chemical reduction, electrochemical, and solvothermal methods [18-22]. However, these methods are typically specialized for a specific composition, structure, and morphology. In the case of Bi<sub>2</sub>O<sub>3</sub>, there are five crystallographic polymorphs: monoclinic ( $\alpha$ -Bi<sub>2</sub>O<sub>3</sub>), tetragonal ( $\beta$ -Bi<sub>2</sub>O<sub>3</sub>), bcc ( $\gamma$ -Bi<sub>2</sub>O<sub>3</sub>), and fcc ( $\delta$ -Bi<sub>2</sub>O<sub>3</sub>). Additionally, bismuth tends to react with CO<sub>2</sub> to form bismuth oxide carbonate and bismuth oxide carbonate hydroxide with an orthorhombic crystal structure.

Bismuth has previously been employed as a PLAL target in a variety of liquid environments and demonstrated some tunability in the composition, structure, and morphology of the resultant nanostructures [23–38]. Dadashi et al. have shown that ablating bismuth in acetone yields pure bismuth nanoparticles with excellent colloidal stability [24]. Another study involving methanol, ethanol, and ethyl methyl ketone (EMK) as ablation liquids resulted in  $\alpha$ -Bi<sub>2</sub>O<sub>3</sub>,  $\beta$ -Bi<sub>2</sub>O<sub>3</sub>, and pure bismuth nanoparticles, respectively [24]. Intriguingly, Morales-Ramos et al. discovered that ablating a bismuth target submerged in an aqueous sodium hypochlorite solution produced metastable  $\gamma$ -Bi<sub>2</sub>O<sub>3</sub> nanoparticles [35]. Ablations in water yield a variety of compositions and morphologies. Dadashi et al. found nanostructures composed of a mixture of bismuth,  $\alpha$ -Bi<sub>2</sub>O<sub>3</sub>,  $\beta$ -Bi<sub>2</sub>O<sub>3</sub>, and Bi(OH)<sub>3</sub> and noted that the nanoparticles continued to oxidize in solution after ablation [25]. Geoffrion et al. conducted high fluence (~160 J/cm²) ablations of

bismuth in water and identified nanosheets composed of both  $\alpha\text{-Bi}_2O_3$  and  $\gamma\text{-Bi}_2O_3$  [31]. In both cases, the resulting compositions were linked to the production of free radicals (O, OH, H ions) in solution during particle ablation. Flores-Castaneda et al. discovered that aging bismuth nanoparticles produced in an aqueous solution resulted in a transition to  $\beta\text{-Bi}_2O_3$  and eventually to  $\text{Bi}_2O_2\text{CO}_3$  nanosheets [25,30]. These examples indicate that laser fluence and liquid environment significantly influence the composition and morphology of the resulting nanostructures.

This study aims to identify factors that result in three distinct bismuth-based nanostructures (BiNSs): bismuth nanospheres, bismuth oxide nanowires, and bismuth oxide carbonate nanosheets. The effects of laser fluence, dissolved gas content (including oxygen and carbon dioxide), and in-solution aging of BiNSs are examined. To alter the dissolved gas content, deionized water is used as the ablation solvent; it is either maintained at ambient conditions, depressurized to remove most of the dissolved gases, or saturated with CO<sub>2</sub>. Furthermore, the sequence of events leading to their formation is investigated.

#### 2. Methods and materials

Ablation took place in a custom-built stainless-steel chamber equipped with an optical port for the introduction of the laser beam and additional side ports for evacuating or introducing pressurized gas. The target surface was irradiated using an EKSPLA model NL-303 Nd:YAG pulsed laser (1064 nm, 5 ns) by focusing the beam with a 75 mm focal length converging lens to a spot size of 600  $\mu m.$  The bismuth targets were produced by pressing 1.5 g of bismuth powder into a 1 cm diameter pellet with 15,000 lb of force for 24-h and its surface sanded prior to ablation. The bismuth pellet was submerged in 15 mL of DDI water and placed on a porated stainless-steel stage above a magnetic stir bar. The liquid height above the target was 13 mm. All ablations took place for a duration of 10 min. Colloidal samples were produced at the following fluences 6, 10, 15, 20 J/cm<sup>2</sup>. The head space above the liquid was held at one of the following 3 states: (1) ambient conditions, (2) evacuated to remove dissolved gases from the ablation solution, or (3) pressurized with CO<sub>2</sub> to saturate the liquid. In cases where the chamber was evacuated, the head space was held at a pressure of -25 inHg for a period of 30 min prior to (and during) ablation. In the case where CO2 was introduced to the chamber, first a constant stream of gas was allowed to bubble through the ablation solution for period of 5 min, then the exhaust port of the chamber was closed, and the pressure allowed to climb to +25 inHg, relative to standard atmospheric pressure. The chamber remained in this state for 30 min prior to ablation. In all instances, immediately after ablation the colloids were transferred under ambient conditions into a glass vial for storage and use in subsequent characterization.

Drop-cast films of the synthesized BiNSs were produced by removing aliquots from the storage vials at specific times post-ablation and transferring them to a falcon tube, where they were centrifuged for 2.5 h at 4900 rpm. The supernatant was then removed, and the concentrated colloid was drop-cast onto a silicon wafer (unless otherwise indicated) and stored in a vacuum chamber. Extinction spectra of the produced BiNS colloids were periodically measured over 24 h using a Carry 60 UV–Vis spectrometer. Before each measurement, the colloid was agitated to resuspend any settled material. Diffuse reflectance spectra were collected from the films using an Ocean Optics SD2000

fiber optic spectrometer, and the optical band gaps extracted using the Tauc plot method. Micro-Raman spectra of the drop cast BiNSs were collected using a Horiba XploRA plus Raman microscope. A laser wavelength of 532 nm and a diffraction grating with 1800 line/mm were used for all measurements. These samples were also investigated via attenuated total internal reflection - Fourier transform infrared spectrometer (ATR-FTIR) using a Bruker ALPHA-Platinum spectrometer. Structure and composition was characterized using a Bruker General Area Detector Diffraction System (GADDS) with a Vantec 500 area detector. For all measurements the detector was centered at  $2\theta = 38^{\circ}$ and the sample was rotated over an angle of  $\Omega=15^{\circ}$  over 900 s. The x-ray diffraction (XRD) patterns were analyzed using the Jade software package to perform Rietveld Refinement and extract the structural and compositional makeup of the BiNSs. The morphological changes to the BiNSs were characterized with an Asylum Research MFP-3D atomic force microscope (AFM). BudgetSenors tap150AI-G AFM tips were used while maintaining a 14 nm x, y-resolution. The BiNSs were drop casted on freshly cleaved mica and placed into a vacuum chamber directly after the ablation process, 3 h after the ablation, and 24 h after the ablation to study the evolution of the BiNSs in solution following the ablation process.

A JOEL 2100Plus transmission electron microscope (TEM) equipped with a 4k Rio Camera (Gatan) was employed to investigate the structure and morphology of the BiNSs following the ablation process by drop casting the BiNSs on a lacey carbon covered copper TEM grid (400 mesh, Ted Pella). Selective area fast Fourier transform (FFT) was performed to investigate the lattice structure of the BiNSs. To facilitate imaging via cryogenic transmission electron microscopy (cryo-TEM), the samples were vitrified using a manual plunge freezer (EMS, model EMS-001), where 5  $\mu$ L of the sample was pipetted onto a lacey carbon covered copper TEM grid (400 mesh, Ted Pella). Front side blotting was manually performed with filter paper, followed by immediate plunging into liquid ethane cryogen maintained at  $-180\,^{\circ}$ C. The grids were then transferred to a Gatan ELSA single-tilt cryo-holder prior to imaging at 200 keV with a magnification of 30,000x.

#### 3. Results

The results discussed below pertain to three different liquid environment conditions that allow control over the dissolved gas content in the ablation liquid. Evacuating the headspace above the liquid assists in removing dissolved O2 and CO2, while ablation without vacuum maintains these levels at ambient conditions. The final environment studied involves introducing CO2 gas into the chamber, thereby saturating the liquid with increased amounts of carbon dioxide. Modifying the liquid environment in this way alters the chemical reactions occurring between the ejected material and the ablation liquid. The type and course of the reactions can be further altered by the laser fluence, which directly influences the temperature of the plasma plume [39,40], and the formation of free radicals. These primary nanoparticles and the liquid state present immediately after ablation state provide the initial conditions for the self-assembly of various nanostructures. To examine the evolution of these primary nanoparticles into higher order nanostructures, a combinational approach was taken to study their composition, morphology, structure, and optical properties over a 24-h period following ablation.

## 3.1. Vibrational spectroscopy

Fig. 1a–c display the micro-Raman spectra collected at 3 different sample locations three hours post-ablation for fluences at 6 and 20  $\rm J/cm^2$  produced in each of the liquid environments. Laser fluence and liquid environment are both shown to significantly influence compositional uniformity throughout the samples. For example, as shown in the lower portion of Fig. 1a, three distinct vibrational spectra are readily found for samples produced at low fluence and in evacuated

conditions. The upper, middle, and lower spectra can be primarily attributed to  $\alpha$ -Bi<sub>2</sub>O<sub>2</sub> (54, 118, 136, 150, 181, 209, 280, 311, 411, and 445 cm<sup>-1</sup>), bismuth carbonate oxide (71, 160, and 367 cm<sup>-1</sup>), and rhombohedral metallic bismuth (69 and 95 cm<sup>-1</sup>), respectively [41,42]. This variation is also observed in samples produced with 20 J/cm<sup>2</sup> in evacuated conditions and 6 J/cm<sup>2</sup> in ambient conditions. For high fluence ambient ablations, samples display better spatial uniformity in terms of composition with  $\alpha$ -Bi<sub>2</sub>O<sub>3</sub> being the most prominent spectral contributor. Samples produced in a CO2 saturated environment are also highly uniform with bismuth carbonate oxide being the primary contributor, though at lower fluence, metallic bismuth also appears. To investigate the influence of aging, micro-Raman spectra were measured on samples drop cast after 24 h, as shown in Fig. 1d. The micro-Raman spectra of samples produced in an evacuated chamber and in ambient conditions align with  $\alpha$ -Bi<sub>2</sub>O<sub>3</sub>, indicating that the ejected nanomaterial has undergone a substantial degree of oxidation at this point. Conversely, samples produced in a CO2 saturated environment do not show significant changes from samples drop cast at earlier times, suggesting that there is minimal to no compositional evolution occurring during the period between 3–24 h post-formation.

Fig. 1e-h depicts the ATR-FTIR spectra of the bismuth nanomaterial films across liquid and fluence conditions at the 3- and 24-h mark. After 3 h, all samples display some combination of the following peaks at approximately 422, 540, and 845, and 1385 cm<sup>-1</sup> which are often assigned to bismuth metal-oxygen stretching modes [43–48]. Samples produced in a saturated CO<sub>2</sub> solution display peaks indicative of carbonate with modes located at 690 cm<sup>-1</sup> (in-plane deformation  $v_4$ ), 845 cm<sup>-1</sup> (out of plane bending  $v_2$ ), 1045 cm<sup>-1</sup> (symmetric vibration  $v_1$ ), and both 1385 and 1447 cm<sup>-1</sup> (antisymmetric stretching  $v_3$ ) [45]. Note, the simultaneous dual assignment of modes at 845 and 1385 cm<sup>-1</sup> can create uncertainties in their respective origin. Bismuth oxide has a propensity for the adsorption of dissolved CO2 [48], hence the presence of these carbonate peaks in the evacuated and ambient samples. These samples also contain a shoulder at ~1540 cm<sup>-1</sup>, attributed to OH bending, and a peak at 1640 cm<sup>-1</sup>, associated with the stretching of Bi-OH, with both peaks increasing in strength with fluence [45,49]. For samples drop-cast 24 h post-ablation, those formed in a CO<sub>2</sub>-saturated environment exhibit little variance, while both ambient and evacuated samples display marked evolution. For example, the peak at 1045 cm<sup>-1</sup> associated with carbonate ions along with the hydroxide peaks are no longer present after 24 h.

#### 3.2. X-ray diffraction

X-ray diffraction was collected from the drop-cast films and analyzed using the Rietveld refinement method. Four different compositions were considered: rhombohedral bismuth (ICDD 01-085-1329), monoclinic bismuth oxide [Bismite  $\rm Bi_2O_3$ ] (ICDD 00-041-1449), orthorhombic bismuth oxide carbonate [bismuth subcarbonate  $\rm Bi_2O_2CO_3$ ] (ICDD 01-084-1752), and bismuth oxide carbonate hydroxide [(BiO)\_4  $\rm CO_3(OH)_2$ ] (ICDD 00-038-057). Fig. 2 depicts the compositional makeup of the samples according to fluence across all three liquid environments. These results are for samples drop-cast 3 h post-ablation. Samples were produced in replicates of four and each analyzed in the same manner. Subsequent results were averaged, with the composition percentages for both the carbonate species summed together.

Under ambient conditions (Fig. 2b), lower ablation fluences (6 and 10 J/cm²) yield nanomaterial with a larger bismuth content (~45%) compared to higher fluences (15 and 20 J/cm²), where the bismuth content reduces to below 30%. At these higher fluences, the percentage of  $\alpha\text{-Bi}_2\mathrm{O}_3$  notably increases, while bismuth carbonate remains relatively consistent. Fig. 2a presents the evacuated environment with a reduced percentage of dissolved gases. Here, the percentages of bismuth,  $\alpha\text{-Bi}_2\mathrm{O}_3$ , and bismuth carbonate species remain relatively stable up to 15 J/cm². Beyond this point, the  $\alpha\text{-Bi}_2\mathrm{O}_3$  composition rises from roughly 10% to 45%, accompanied by decreases in metallic and

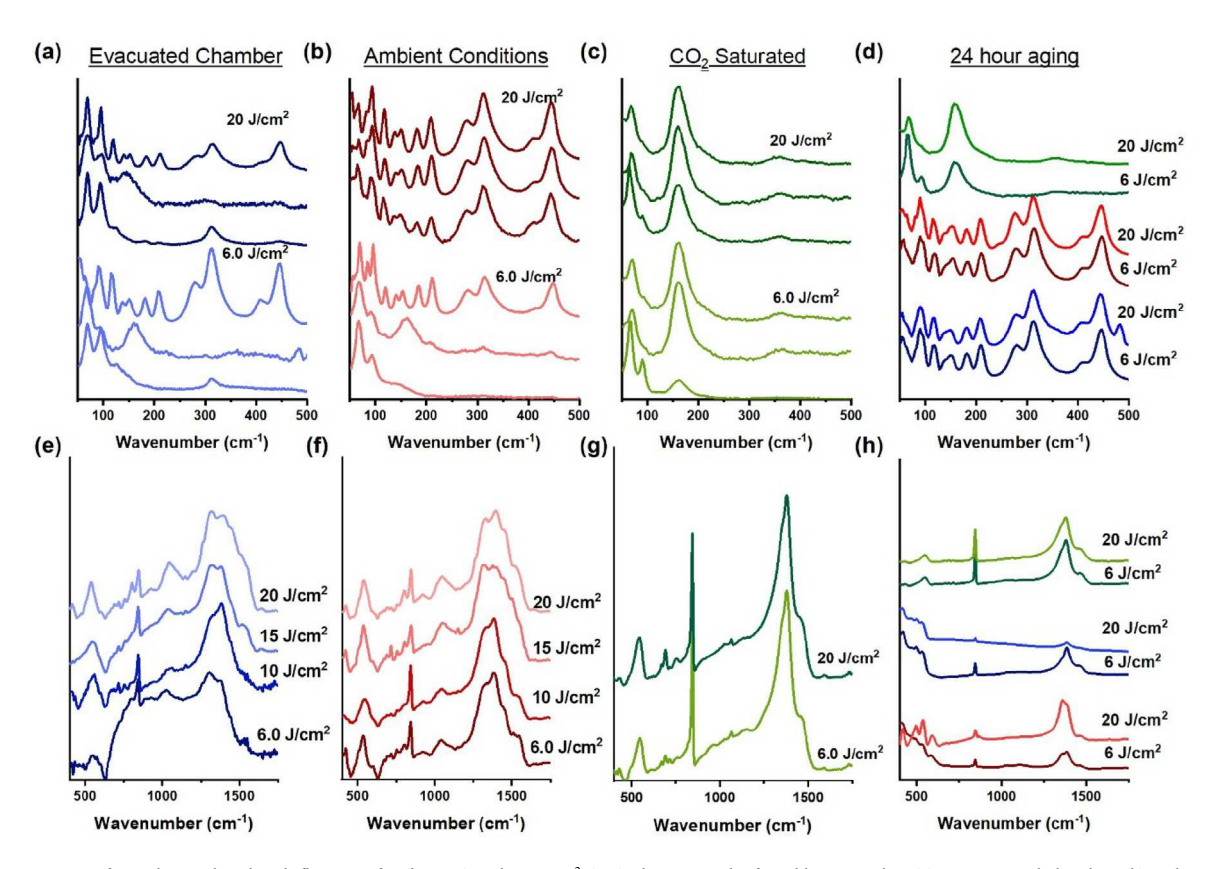


Fig. 1. Raman spectra of samples produced with fluences of 6 (bottom) and 20 J/cm<sup>2</sup> (top), drop cast 3 h after ablation, and in (a) an evacuated chamber, (b) ambient conditions, and (c)  $CO_2$  Saturated conditions. (d) Raman spectra of samples drop cast 24 h after ablation. ATR-FTIR spectra of samples produced with fluences of 6, 10, 15, 20 J/cm<sup>2</sup> and drop cast 3 h after ablation and in (e) an evacuated chamber, (f) ambient conditions, and (g)  $CO_2$  Saturated conditions. (h) ATR-FTIR spectra of samples drop cast 24 h after ablation.

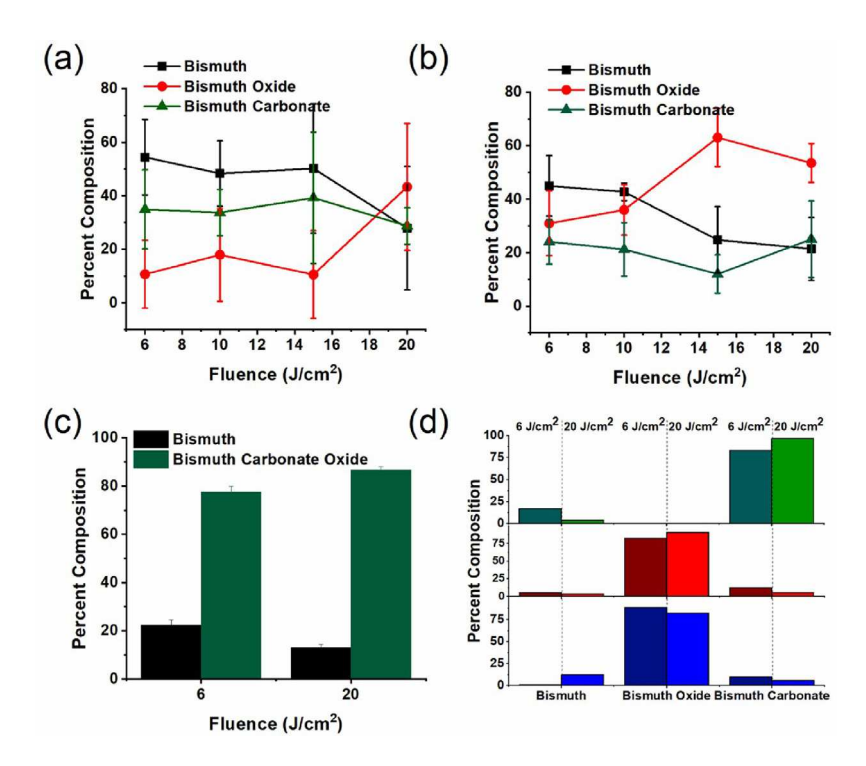


Fig. 2. Percent composition of samples drop cast 3 h after ablation and produced in (a) an evacuated chamber (b) ambient conditions, and (c) CO<sub>2</sub> saturated conditions. (d) percent composition of samples drop cast 24 h after ablation for samples produced in an evacuated chamber (blue), ambient conditions (red), and CO<sub>2</sub> saturated conditions (green).

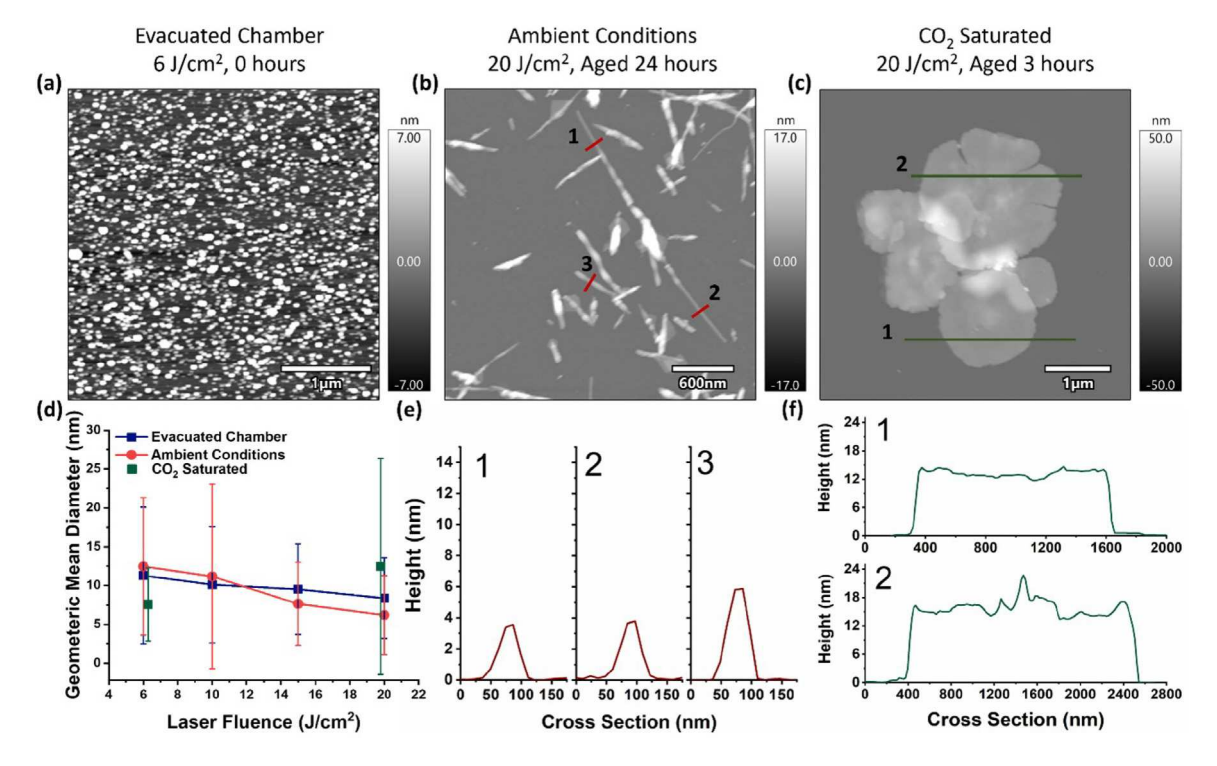


Fig. 3. AFM images of samples produced in (top left) an evacuated chamber with a fluence of 6  $J/cm^2$  and drop casted directly after ablation, (top middle) in ambient conditions with a fluence of 20  $J/cm^2$  and drop cast 24 h after ablation, and (top right) in  $CO_2$  saturated conditions and drop cast 3 h after ablation. (bottom left) Height analysis of particles drop cast directly after ablation. (bottom middle) cross section of nanowires. (bottom right) Cross section of nanosheets.

carbonate bismuth. For the  $CO_2$  saturated liquid environment (Fig. 2c), only bismuth and bismuth oxide carbonate are discernible in the XRD patterns. Notably, carbonate samples displayed a preferred (010) orientation. The nanomaterial predominantly consists of bismuth oxide carbonate at both low and high fluence levels, with compositions of about 80% and 90%, respectively. Fig. 2e depicts the composition of the drop-cast films at the 24-h mark. Samples produced under both ambient conditions and in an evacuated chamber are primarily  $\alpha$ -Bi<sub>2</sub>O<sub>3</sub>, while percentages of both bismuth and bismuth subcarbonate decrease compared to 3-h post-ablation samples. However, nanostructures formed in a  $CO_2$  saturated environment showed little variation compared to the 3-h samples.

#### 3.3. Atomic force microscopy

Evolution of the size and morphology of the nanomaterials was investigated using AFM, see Fig. 3. Samples were produced by dropcasting the colloid onto freshly cleaved mica for time intervals of 0-, 3-, and 24-h post-ablation. As shown in Fig. 3a, the combination of low fluence and an evacuated chamber results in spherical particles immediately after ablation; this trend extends to the other conditions as well irrespective of fluence or liquid environment. The particle size, determined by measuring their maximum height, displayed a lognormal distribution skewed towards larger sizes, a trend typically observed in PLAL-produced nanoparticles. The geometric mean and standard deviation of the resulting nanoparticles are presented in Fig. 3d across all fluence and liquid conditions. Particles produced under ambient and vacuum conditions both trend towards a decrease in mean diameter and standard deviation with increasing fluence. Samples produced with a fluence of 6 J/cm<sup>2</sup> under ambient and evacuated conditions had mean diameters of  $12 \pm 9$  nm and  $11 \pm 9$  nm, respectively. Upping the fluence to 20 J/cm<sup>2</sup> resulted in particles with mean diameters of 6.2  $\pm$  5.1 nm and 8.4  $\pm$  5.2 nm, respectively. BiNPs produced in

 $CO_2$ -saturated DDI immediately after ablation measured 9.2  $\pm$  4.4 nm and  $13 \pm 12$  nm for fluences of 6 and 20 J/cm<sup>2</sup>, respectively. Besides spherical particles, several nanosheets were also identified in the CO2 samples. By the 3-h mark, samples produced low fluences in evacuated and ambient environments retained their spherical nature. However, at higher fluences, the presence of higher-order nanostructures becomes evident, especially in ambient samples. By the 3-h mark, samples produced under ambient conditions at 20 J/cm<sup>2</sup> comprise of a mix of spherical particles, nanowires, and nanosheets. However, by 24 h this sample predominately consists of a network of elongated nanowires (nanobundles) with a mean diameter (height) of 6.9  $\pm$  2.4 nm, as shown in Fig. 3b. In addition to nanoparticles, primitive nanosheets produced in CO<sub>2</sub>-saturated solution are observed as seen in figure S11. The average thickness of the sheets was measured at  $11 \pm 4.3$  nm, with the minimum being 2.7 nm. This minimum correlates to the caxis of the unit cell of orthorhombic bismuth oxide carbonate [50]. At 3 h, samples created in a CO2-saturated solution primarily consist of nanosheet structures with a mean thickness of  $14 \pm 3.4$  nm and a width ranging from 0.25 to 2.5  $\mu m$ , as shown in Fig. 3c and f. By 24 h, the nanosheet structures persist, but some have further evolved into flowerlike structures. For both evacuated and ambient sample produced at low fluences the initial spherical shape of the nanomaterial persists over the entire 24 period.

# 3.4. Transmission electron microscopy

The colloidal solutions were drop cast onto TEM grids at 0-, 3-, and 24-h after ablation to study changes in structure and morphology over time. Fig. 4 presents representative TEM images of the resulting nanomaterials across all three intervals and environmental conditions. Under low fluence with an evacuated headspace, the resulting material consists primarily of isolated spherical particles immediately after ablation, corroborating the AFM results. By 3 h, these spherical particles

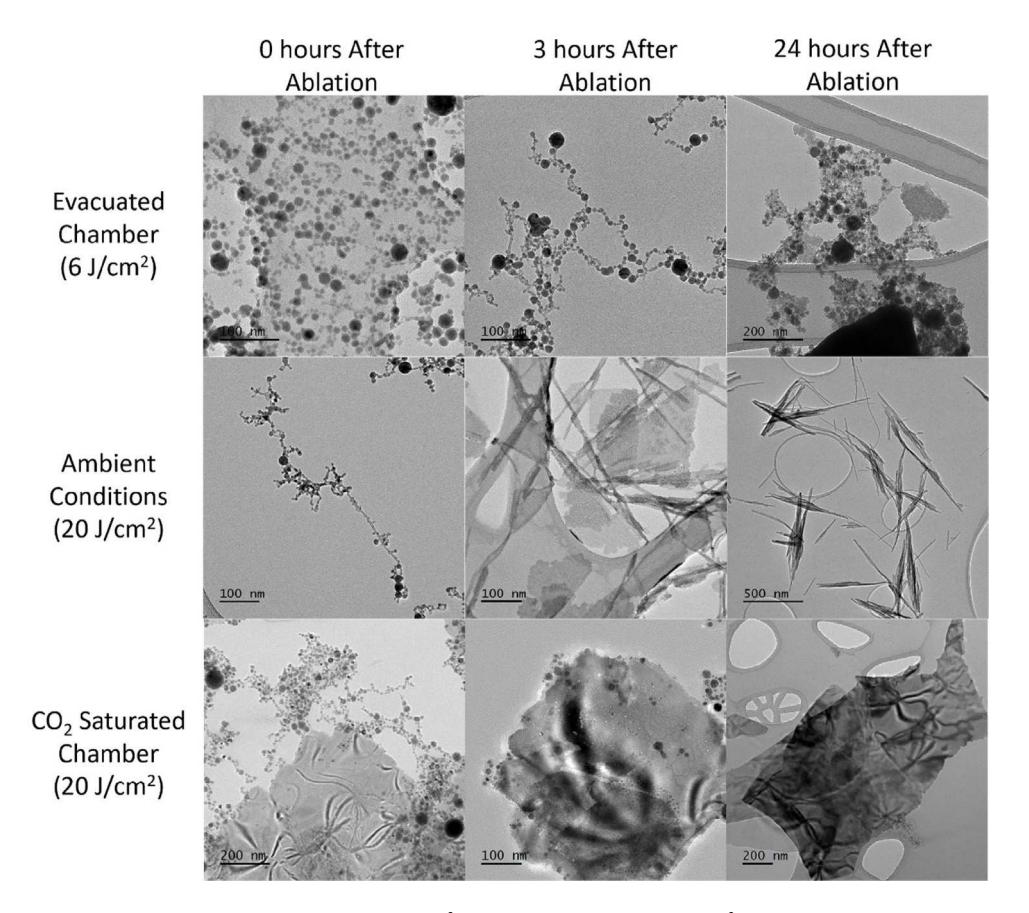


Fig. 4. TEM images of samples produced in an evacuated chamber with 6 J/cm<sup>2</sup>, ambient conditions with 20 J/cm<sup>2</sup>, and CO<sub>2</sub> saturated conditions that were drop cast directly after, 3 h after, and 24 h after ablation.

have evolved into stranded bead-like aggregates in addition to several nanosheets that can be found throughout the sample, see supplementary Figure S6. And finally at 24 h, the nanomaterial has formed into relatively low-order aggregates in the absence of nanowires. For high fluence ambient ablations at the 0-h mark, in addition to spherical particles, nascent nanowires are also present in the drop-cast samples. By 3 h, a significant deviation from the aforementioned trends in the evacuated case occur, with the nanomaterial evolving into a mixture of mature nanowires that have aligned to form nanobundles, which are accompanied by square nanosheets with lateral dimensions ranging from 100-200 nm. Strikingly, at 24 h, the primary structures present are the nanobundles with both the spherical particles and nanosheets now absent. Under low fluence ambient conditions, results are comparable to those in the evacuated case with the sample being mostly composed of spherical nanoparticles, but with a slightly higher degree of particle-to-particle organization, as seen in Figure S6. Three hours post-ablation, TEM images depict a blend of large amorphous aggregates, bead-like aggregates, and nanosheets. When the ablation solution is saturated with CO2, the result is predominantly sheet-like structures with a minority of spherical particles, regardless of the fluence level (6 or 20 J/cm<sup>2</sup>). In samples drop cast 3 h post-ablation, a decrease in spherical nanoparticles is noted, with square nanosheets, averaging  $750 \pm 470$  nm in length, becoming the dominant nanostructure. By the 24-h mark, samples prepared at 20 J/cm<sup>2</sup> lack spherical nanoparticles, and many of the nanosheets have aggregated.

High-Resolution TEM was employed to discern the lattice structures of the various observed nanostructure types, such as nanobundles and nanosheets. These were then compared with XRD results to ascertain their composition. Fig. 5a showcases a HR-TEM image of a representative spherical particle from an ablation at 6 J/cm² in an evacuated chamber. Clear lattice fringes are visible. The FFT of this region (refer to the inset) reveals a lattice spacing of 3.27 Å in the (012) direction,

characteristic of rhombohedral (metallic) bismuth. Colloids generated in ambient conditions at 20 J/cm<sup>2</sup> immediately post-ablation are primarily spherical particles. However, these particles are now encased in an amorphous oxide shell (as seen in Fig. 5b) with a metallic bismuth core. The FFT analysis of the core displays spacings of 1.96 and 3.98 Å in the (003) and (006) directions, respectively. Fig. 5c provides an HR-TEM image of a nanowire formed 3 h post-ablation under ambient conditions at 20 J/cm<sup>2</sup>. The image elucidates that the nanowire consists of spherical particles set within a crystalline matrix. The red inset confirms that the high-contrast spherical particles are metallic bismuth. Meanwhile, the blue inset highlights FFT for the lower contrast regions of the wire, where lattice spacings of 2.74 and 3.19 Å were determined. These spacings correspond to scattering along the (-211) and (012) directions of monoclinic bismuth oxide, respectively. Lastly, Fig. 5d depicts a nanosheet created in a CO2 saturated solution. The nanosheet displays the presence of fringing, with FFT analysis indicating lattice spacings of 2.74 and 1.94  $\hbox{\normalfont\AA}$  in perpendicular orientations. This suggests that the nanosheets are bismuth carbonate oxide and the presence of the observed reflections indicates an orientation along the [010] plane.

### 3.5. Cryo-TEM

Samples produced under ambient conditions experience significant changes over a 24-h period. Therefore, cryo-TEM was specifically used to image these samples at an intermediate seven-hour post-ablation stage. Cryo-TEM images a vitrified thin layer of solution hence preserving the sample in its naturally hydrated state. This technique can provide insight into the event sequence of nanostructure formation. In Fig. 6a-c, three distinct stages of spherical nanoparticle aggregation and nanosheet formation can be observed. Fig. 6a presents a 2D aggregate with metallic bismuth NPs interspersed within a lower contrast matrix, likely consisting of bismuth subcarbonate. Fig. 6b illustrates

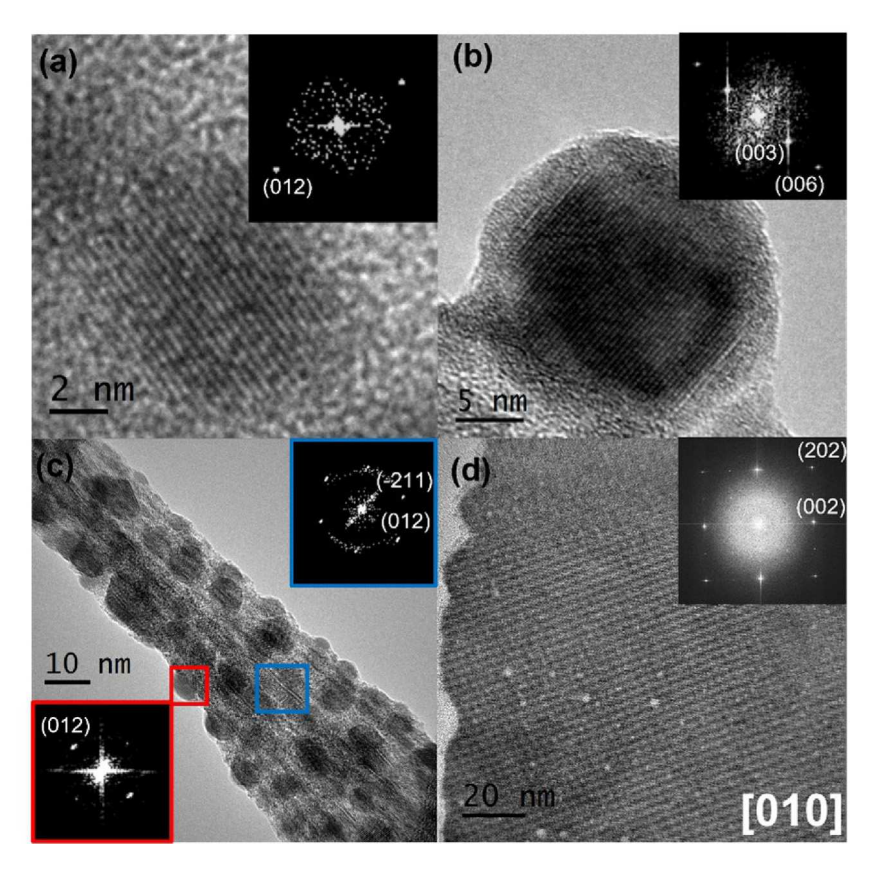


Fig. 5. HR-TEM images of (a) nanoparticle produced in an evacuated chamber with 6  $J/cm^2$  drop cast directly after, (b) nanoparticle produced in ambient conditions with 20  $J/cm^2$  drop cast directly after ablation, (c) nanowire produced in ambient conditions with 20  $J/cm^2$  and drop cast 24 h after, and (d) nanosheet produced in  $CO_2$  saturated conditions with 20  $J/cm^2$  and drop cast 3-h after ablation.

a more evolved aggregate, with a small (approximately  $20 \times 10$  nm) rectangular sheet visible at the top. Fig. 6c portrays a rather developed nanosheet with consistent contrast across its expanse. These nanosheets ultimately give way to nanobundles as shown in Fig. 6d where bundle growth is shown to take place around the perimeter of the sheet along perpendicular directions. Separately, nanowires (nanobundles) can also be found throughout the sample which originate directly from the NPs and do not appear to require an intermediary nanosheet phase, as demonstrated in Fig. 6e.

## 3.6. Optical properties

The optical properties and aging of the colloids were studied by collecting UV-Vis spectra immediately after ablation and periodically over a 3-h span, as shown in Fig. 7a. It is worth noting that these extinction spectra are a combination of absorption and scattering from the nanostructures in solution. All samples display some degree of spectral evolution and a net absorbance decrease over time; however, the change is more pronounced in some samples compared to others. The most pronounced absorbance change occurs at approximately 360 nm, especially in the ambient sample. Fig. 7b depicts the optical absorbance at 360 nm for ablations at 20 J/cm<sup>2</sup> across all three liquid environments. This plot distinctly shows that the colloid produced under ambient conditions experiences the most significant spectral evolution. This aligns with TEM and AFM analyses, which demonstrate that this sample transitions from spherical nanoparticles to a blend of nanowires and nanosheets. In contrast, the evacuated samples, which primarily remain spherical, and the CO<sub>2</sub>-saturated colloid, which rapidly transforms into nanosheets, evolve far less over the 3-h period. This correlation between spectral evolution and morphological changes, as observed in TEM (and/or AFM), is consistent across all other fluences, as seen in Figure S11.

Diffuse reflectance spectroscopy was conducted on samples at 3and 24-h post-ablation, the results of which are shown in Fig. 8. Interestingly, the spectra indicate two distinct absorption edges, suggesting the presence of different bismuth-based compounds. By analyzing the first derivative of these spectra, the absorption edges were located at approximately 348 and 425 nm, aligning well with the literature band gap values for bismuth oxide carbonate and  $\alpha$ -Bi<sub>2</sub>O<sub>3</sub>, respectively [51,52]. Both low and high fluence samples, produced in an evacuated chamber, exhibit a redshift in the absorption edge. This change can likely be attributed to a decrease in carbonate species in favor of  $\alpha$ -Bi<sub>2</sub>O<sub>3</sub>, occurring over the 3- to-24-h span. A similar trend was observed in high-fluence samples under ambient conditions, however a more well-defined edge, located at 428 nm, emerged after 24 h, indicative of a transition to  $\alpha$ -Bi<sub>2</sub>O<sub>3</sub>. The spectra associated with CO<sub>2</sub> saturated samples show little spectral evolution over this time span for all fluences.

To further investigate the corresponding bandgap energies, the Tauc plot method was employed for those spectra displaying a well-defined edge. Bismuth oxide is considered a direct band gap semiconductor, as such  $(\alpha h \nu)^2$  was plotted against photon frequency for both the ambient high fluence and evacuated low fluences samples at 24 h. Linear extrapolation to the horizontal axis yielded bandgap energies of 2.91 eV and 2.88 eV, respectively, which is in line with 2.89 eV associated with monoclinic bismuth oxide. For  $CO_2$ -saturated samples, considered to be indirect in nature according to literature, an exponent of 1/2 was used in the plots. The resulting bandgap energy measurement of 3.44 eV aligns well with existing literature values of approximately 3.42 eV [52].

#### 4. Discussion

The results discussed above provide evidence that factors such as laser fluence, environmental conditions in the ablation chamber,

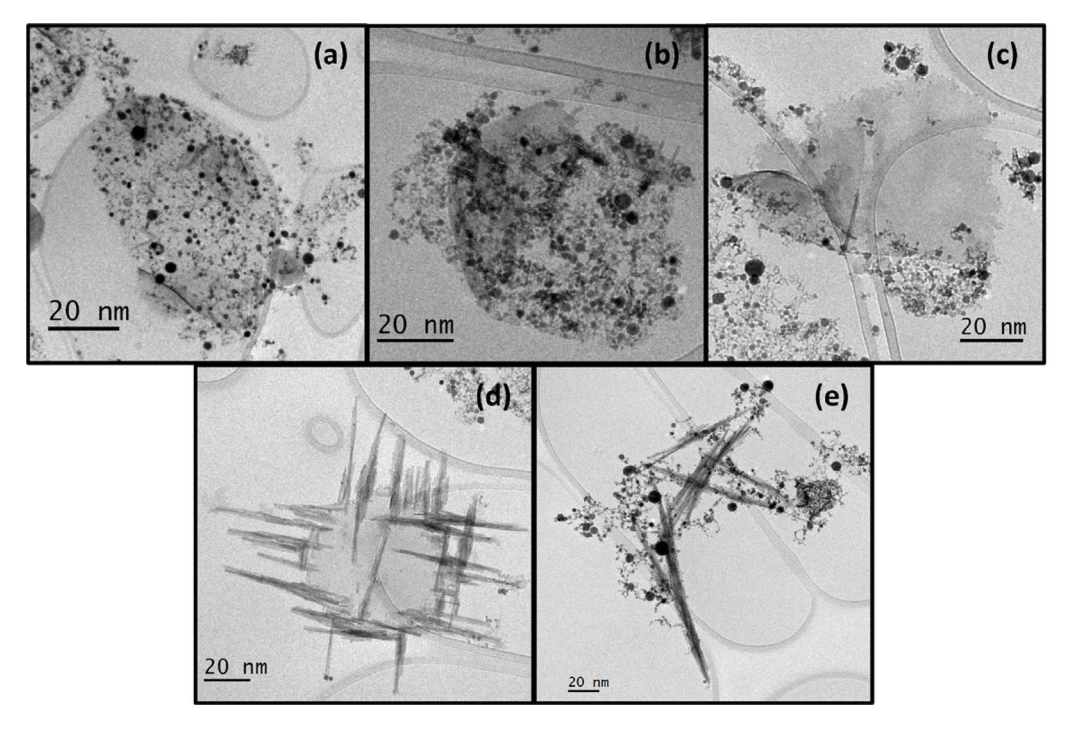


Fig. 6. (a-f) Cryo-TEM images of nanostructures produced in ambient conditions with a fluence of 20 J/cm<sup>2</sup> and vitrified 7-h after ablation.

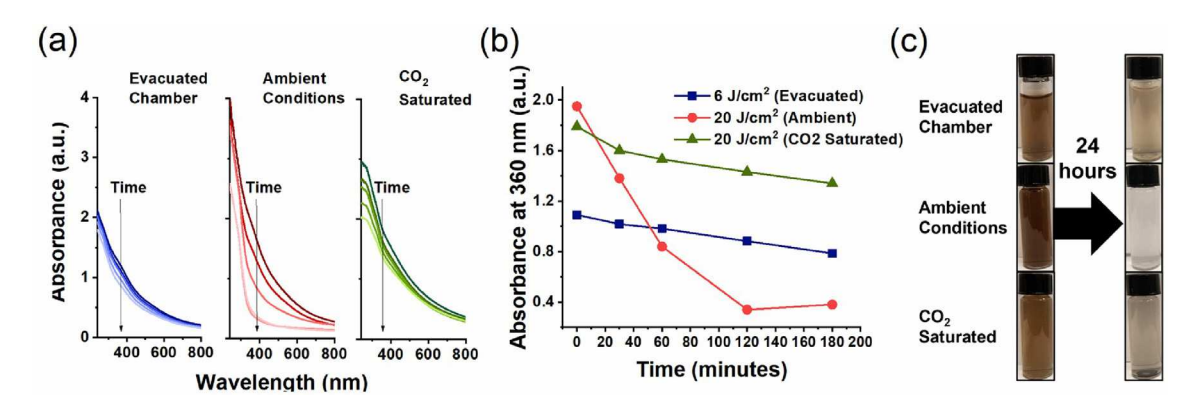


Fig. 7. (a) UV-Vis spectra over the course of 3 h following the ablation. (b) The absorbance at 360 nm plotted as a function of time. (c) Pictures of the colloid directly after and 24-h after the ablation.

and colloid aging, significantly influence BiNS morphology and composition. The formation of BiNS appears to occur in two sequential stages. First, spherical primary particles, smaller than 15 nm, form immediately after ablation, as verified by TEM and AFM. Subsequently, these particles may interact with their surroundings, leading to the development of more complex structures, such as nanowire bundles and nanosheets. The composition and surface chemistry of these primary particles heavily influence their trajectory during the second phase, dictating their final composition and morphology. Within the initial hours after ablation, drastic changes in the extinction spectra are observed for high fluence colloids produced under ambient conditions. However, colloids produced in a  $\rm CO_2$  saturated environment remain fairly consistent. Analysis via HRTEM shows that these primary particles typically have a metallic bismuth core surrounded by an amorphous oxide shell.

By the 3-h mark post-ablation, various characterization techniques, including vibrational spectroscopy, DRS, and XRD, reveal the presence of  $\alpha\textsc{-Bi}_2O_3$  and bismuth oxide carbonate in samples from vacuum and ambient ablations. In contrast, the  $CO_2$  saturated environment predominantly produces bismuth oxide carbonate nanostructures. Notably,

in CO<sub>2</sub> saturated conditions, this carbonate remains stable over 24 h, but other conditions exhibit significant evolution. The most striking of which occurs in high fluence samples under ambient conditions. By the 3-h mark, an amalgamation of  $\alpha$ -Bi<sub>2</sub>O<sub>3</sub> nanowire bundles and carbonate nanosheets, originating from the primary core-shell nanoparticles, is evident. Geoffrion et al. discussed the propensity for bismuth oxides to adopt 1 and 2D structures, rather than the typical spherical structures. It was suggested that the overall growth is determined by two competing factors, minimization of the surface to volume ratio as well as the surface energy. In cases, where the surface energy of the solvent is greater than that of the particles, 1 and 2D structures are likely to form, while conversely the system minimizes the surface to volume ratio by forming spherical particles [30]. In this case, bismuth oxide has a lower surface energy than water which explains the formation of nanowires, and a similar rationale applies to the development of bismuth carbonate nanosheets.

Upon further aging, the bismuth carbonate nanosheets start to be replaced by nanowire bundles, as illustrated in cryo-TEM images taken

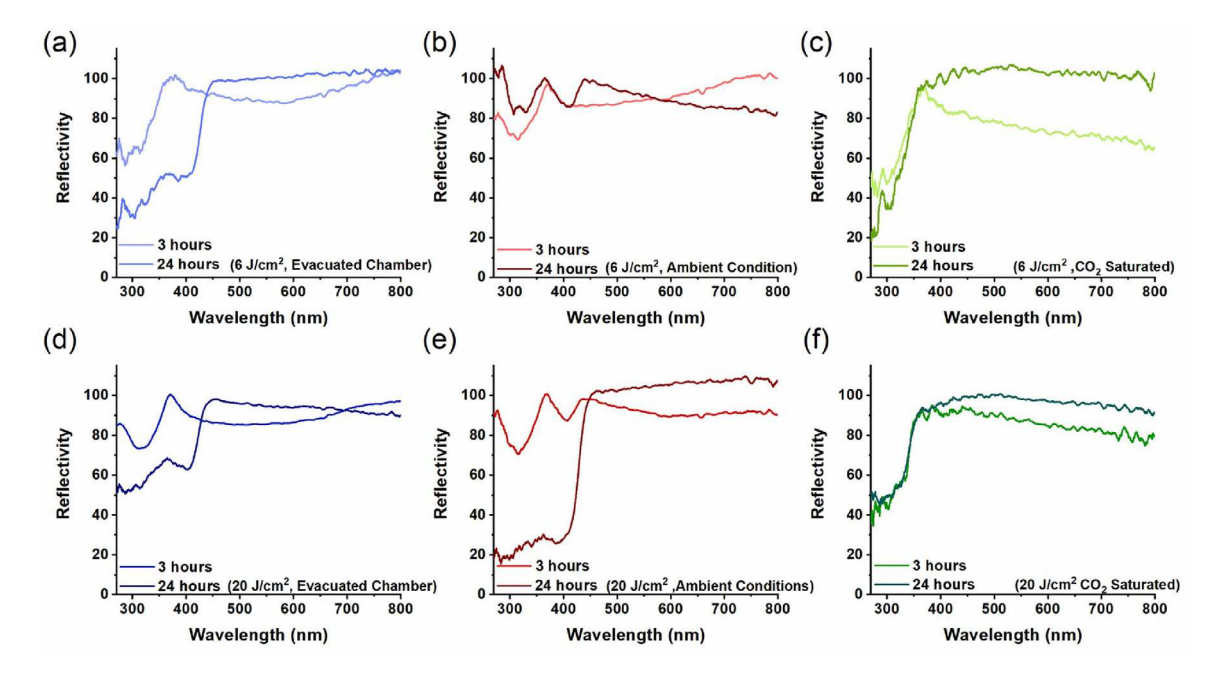


Fig. 8. Reflectivity spectra 3-h and 24-h after ablation for samples produced with 6  $J/cm^2$  in (a) an evacuated chamber, (b) ambient conditions, (c) in  $CO_2$  saturated conditions, as well as samples produced with 20  $J/cm^2$  in (d) an evacuated chamber, (e) ambient conditions, (f) in  $CO_2$  saturated conditions.

at 7 h. These images depict nanowire bundles encircling the sheet's perimeter in perpendicular arrangements. By the 24-h mark, TEM/AFM images indicate that these nanobundles have become the predominant nanostructure. This shift aligns with XRD results, revealing a substantial decrease in bismuth carbonate species at 24 h, and reflectivity data highlighting a distinct  $\alpha$ -Bi<sub>2</sub>O<sub>3</sub> absorption edge. This observation contrasts results reported by Flores-Castaneda et al. who note a transition from a similar nanowire-nanosheet mixture post ablation to a final stable state of Bi<sub>2</sub>O<sub>2</sub>CO<sub>3</sub> nanosheets for PLAL of bismuth in ambient water [29]. The difference in outcome may be attributable to differences in experimental conditions, including the form of the bismuth target (pressed metal powder vs. continuous solid), pulse duration (nanoseconds vs. femtoseconds), concentration of dissolved CO<sub>2</sub>, and fluence (20 vs. 4.77 J/cm²).

The behavior suggests two distinct reaction pathways that end in the formation of bismuth oxide nanowire bundles: (1) oxidation and assembly of the primary particles which leads to direct formation of  $\alpha$ -Bi<sub>2</sub>O<sub>3</sub> nanowires, and (2) CO<sub>2</sub> absorption and assembly of the ablated material in bismuth carbonate nanosheets which ultimately give rise to  $\alpha$ -Bi<sub>2</sub>O<sub>3</sub> nanowires. This system initially favors a non-equilibrium state before stabilizing in a colloid of bismuth oxide nanowire bundles with time. As Taylor et al. have demonstrated, de-carbonation of (BiO)2CO3 and (BiO)4(OH)2CO3 can transpire in an aqueous environment, contingent on the solution's carbonate and hydroxide concentrations, effectively converting the carbonates to monoclinic bismuth oxide. ATR-FTIR spectra of samples produced at higher fluences and drop cast after 3 h detected Bi-OH. Nonetheless, by 24 h, no vibrational modes linked to -OH were discernible in the drop cast samples. The oxide/hydroxide shell's presence on the primary nanoparticles might facilitate the de-carbonation of the nanosheets.

#### 5. Conclusion

The reactive nature of bismuth allows for a more intricate PLAL process as compared with the ablation of noble metals. This reactivity can be leveraged to fine-tune the morphology, composition, and structure of the resulting nanomaterials. Our results demonstrate that dissolved gases, particularly  $\mathrm{CO}_2$  and  $\mathrm{O}_2$ , play a crucial role in PLAL. They not only influence the primary particles formed immediately after ablation,

but also significantly impact the aging process of the colloid. Specifically, the concentration of CO2 markedly affects the post-ablation trajectory of bismuth nanostructures in terms of their composition, structure, and morphology. The removal of dissolved gases like O2 in aqueous environments results in a reduction of oxidized bismuth forms, preserving its metallic state. However, at higher fluences, a threshold is reached where the photothermal breakdown of water becomes an alternative oxygen source. By adjusting PLAL parameters such as laser fluence and dissolved gases, this study identified the conditions required to synthesize one of three distinct bismuth-based nanostructures: core/shell bismuth-bismuth oxide spherical nanoparticles, bismuth oxide nanowire bundles, and bismuth subcarbonate nanosheets. This study underscores the dynamic nature of PLAL in fabricating diverse nanostructures, highlighting its potential for tailored applications in various fields. However, if the technique is to become a viability source of nanomaterials, the relatively low productivity rates associated with PLAL of bulk targets must be overcome. Currently, the highest rates achieved are in the range of a few grams per hour, and they are shown to be highly dependent on various PLAL parameters, including target composition, pulse duration, and repetition rate [53]. Most studies on production rates have been conducted in relatively simple liquid environments with low-reactivity targets such as gold, in contrast to the more complex system of conditions employed in this study.

#### CRediT authorship contribution statement

Cory J. Trout: Writing – review & editing, Writing – original draft, Visualization, Methodology, Investigation, Formal analysis, Data curation, Conceptualization. Robert Albertson: Investigation. Julianne C. Griepenburg: Writing – review & editing, Resources, Project administration, Funding acquisition. Sean M. O'Malley: Writing – review & editing, Writing – original draft, Visualization, Supervision, Resources, Project administration, Methodology, Conceptualization.

#### **Declaration of competing interest**

The authors declare that they have no known competing financial interests or personal relationships that could have appeared to influence the work reported in this paper.

#### Data availability

Data will be made available on request.

# Declaration of Generative AI and AI-assisted technologies in the writing process

During the preparation of this work the Authors used the language model developed by OpenAI in order to improve readability and language. After using this tool/service, the Authors reviewed and edited the content as needed and take(s) full responsibility for the content of the publication.

#### Acknowledgments

The Authors wish to acknowledge the support from National Science Foundation award # 2213408. Additionally, this research utilized microscopy resources supported by the National Science Foundation, United States (award # DMR-1827557) and the Stevens Institute of Technology. The Authors extend their gratitude to Drs. Tsengming (Alex) Chou and Matthew Libera at Stevens Institute of Technology for their assistance in acquiring the TEM images. Furthermore, the Authors are appreciative of Dr. Thomas Emge and the Department of Chemistry and Chemical Biology for their aid in acquiring the X-ray diffraction data.

#### Appendix A. Supplementary data

Supplementary material related to this article can be found online at https://doi.org/10.1016/j.colsurfa.2024.133768.

#### References

- [1] M. Amin, J. Tomko, J. Naddeo, R. Jimenez, D. Bubb, M. Steiner, J. Fitz-Gerald, S. O'Malley, Laser-assisted synthesis of ultra-small anatase TiO<sub>2</sub> nanoparticles, Appl. Surf. Sci. 348 (2015) 30–37, http://dx.doi.org/10.1016/j.apsusc.2014.12.191, Advanced Synthesis of Functional Nanoparticles by Lasers in Liquids From Fundamentals to Application in Catalysis, Energy Science, and Biomedicine.
- [2] F. Mafuné, J.-y. Kohno, Y. Takeda, T. Kondow, H. Sawabe, Formation and size control of silver nanoparticles by laser ablation in aqueous solution, J. Phys. Chem. B 104 (39) (2000) 9111–9117, http://dx.doi.org/10.1021/jp001336y, arXiv:https://doi.org/10.1021/jp001336y.
- [3] M.I. Mendivil Palma, B. Krishnan, G.A.C. Rodriguez, T.K. Das Roy, D.A. Avellaneda, S. Shaji, Synthesis and properties of platinum nanoparticles by pulsed laser ablation in liquid, J. Nanomater. 2016 (2016) 9651637, http://dx.doi.org/10.1155/2016/9651637.
- [4] D. Riabinina, J. Zhang, M. Chaker, J. Margot, D. Ma, Size control of gold nanoparticles synthesized by laser ablation in liquid media, ISRN Nanotechnol. 2012 (2012) 297863, http://dx.doi.org/10.5402/2012/297863.
- [5] V.A. Svetlichnyi, A.V. Shabalina, I.N. Lapin, D.A. Goncharova, D.A. Velikanov, A.E. Sokolov, Study of iron oxide magnetic nanoparticles obtained via pulsed laser ablation of iron in air, Appl. Surf. Sci. 462 (2018) 226–236, http://dx.doi. org/10.1016/j.apsusc.2018.08.116.
- [6] R.K. Swarnkar, S.C. Singh, R. Gopal, Effect of aging on copper nanoparticles synthesized by pulsed laser ablation in water: structural and optical characterizations, Bull. Mater. Sci. 34 (7) (2011) 1363–1369, http://dx.doi.org/10.1007/ s12034-011-0329-4.
- [7] N. Tarasenko, A. Butsen, E. Nevar, N. Savastenko, Synthesis of nanosized particles during laser ablation of gold in water, Appl. Surf. Sci. 252 (13) (2006) 4439–4444, http://dx.doi.org/10.1016/j.apsusc.2005.07.150, Proceedings of the European Materials Research society 2005 Symposium-J: Advances in Laser and Lamp Processing of Functional Materials.
- [8] T. Tsuji, T. Hamagami, T. Kawamura, J. Yamaki, M. Tsuji, Laser ablation of cobalt and cobalt oxides in liquids: influence of solvent on composition of prepared nanoparticles, Appl. Surf. Sci. 243 (1) (2005) 214–219.
- [9] I.Y. Khairani, Q. Lin, J. Landers, S. Salamon, C. Doñate-Buendía, E. Karapetrova, H. Wende, G. Zangari, B. Gökce, Solvent influence on the magnetization and phase of Fe-Ni alloy nanoparticles generated by laser ablation in liquids, Nanomaterials 13 (2) (2023) http://dx.doi.org/10.3390/nano13020227.
- [10] R.M. Tilaki, A.I. zad, S.M. Mahdavi, The effect of liquid environment on size and aggregation of gold nanoparticles prepared by pulsed laser ablation, J. Nanopart. Res. 9 (5) (2007) 853–860, http://dx.doi.org/10.1007/s11051-006-9143-0.

- [11] J. Toudert, R. Serna, C. Deeb, E. Rebollar, Optical properties of bismuth nanostructures towards the ultrathin film regime, Opt. Mater. Express 9 (7) (2019) 2924–2936, http://dx.doi.org/10.1364/OME.9.002924.
- [12] A. Boukai, K. Xu, J. Heath, Size-dependent transport and thermoelectric properties of individual polycrystalline bismuth nanowires, Adv. Mater. 18 (7) (2006) 864–869, http://dx.doi.org/10.1002/adma.200502194, arXiv:https://onlinelibrary.wiley.com/doi/pdf/10.1002/adma.200502194.
- [13] J. Heremans, C.M. Thrush, Thermoelectric power of bismuth nanowires, Phys. Rev. B 59 (1999) 12579–12583, http://dx.doi.org/10.1103/PhysRevB.59.12579.
- [14] J. Toudert, R. Serna, I. Camps, J. Wojcik, P. Mascher, E. Rebollar, T.A. Ezquerra, Unveiling the far infrared-to-ultraviolet optical properties of bismuth for applications in plasmonics and nanophotonics, J. Phys. Chem. C 121 (6) (2017) 3511–3521, http://dx.doi.org/10.1021/acs.jpcc.6b10331, arXiv:https://doi.org/10.1021/acs.jpcc.6b10331.
- [15] Z. Liu, Q. Wang, X. Tan, S. Zheng, H. Zhang, Y. Wang, S. Gao, Solvothermal preparation of Bi/Bi<sub>2</sub>o<sub>3</sub> nanoparticles on TiO<sub>2</sub> NTs for the enhanced photoelectrocatalytic degradation of pollutants, J. Alloys Compd. 815 (2020) 152478, http://dx.doi.org/10.1016/j.jallcom.2019.152478.
- [16] H.-W. Wang, Z.-A. Hu, Y.-Q. Chang, Y.-L. Chen, Z.-Q. Lei, Z.-Y. Zhang, Y.-Y. Yang, Facile solvothermal synthesis of a graphene nanosheet–bismuth oxide composite and its electrochemical characteristics, Electrochim. Acta 55 (28) (2010) 8974–8980, http://dx.doi.org/10.1016/j.electacta.2010.08.048.
- [17] Y.W. Wang, B.H. Hong, K.S. Kim, Size control of semimetal bismuth nanoparticles and the UV visible and IR absorption spectra, J. Phys. Chem. B 109 (15) (2005) 7067–7072, http://dx.doi.org/10.1021/jp046423v, PMID: 16851804. arXiv:https: //doi.org/10.1021/jp046423v.
- [18] L. Balan, R. Schneider, D. Billaud, Y. Fort, J. Ghanbaja, A new synthesis of ultrafine nanometre-sized bismuth particles, Nanotechnology 15 (8) (2004) 940, http://dx.doi.org/10.1088/0957-4484/15/8/011.
- [19] G. Cheng, H. Yang, K. Rong, Z. Lu, X. Yu, R. Chen, Shape-controlled solvothermal synthesis of bismuth subcarbonate nanomaterials, J. Solid State Chem. 183 (8) (2010) 1878–1883, http://dx.doi.org/10.1016/j.jssc.2010.06.004.
- [20] D. Ma, J. Zhao, Y. Zhao, X. Hao, L. Li, L. Zhang, Y. Lu, C. Yu, Synthesis of bismuth nanoparticles and self-assembled nanobelts by a simple aqueous route in basic solution, Colloids Surf. A 395 (2012) 276–283, http://dx.doi.org/10. 1016/j.colsurfa.2011.12.055.
- [21] N. Motakef-Kazemi, M. Rashidian, S.T. Dabbagh, M. Yaqoubi, Synthesis and characterization of bismuth oxide nanoparticle by thermal decomposition of bismuth-based MOF and evaluation of its nanocomposite, Iran. J. Chem. Chem. Eng.-Int. Engl. Ed. 40 (2021) 11–19.
- [22] M. Patil, V. Deshpande, S. Dhage, V. Ravi, Synthesis of bismuth oxide nanoparticles at 100 °C, Mater. Lett. 59 (19) (2005) 2523–2525, http://dx.doi.org/10.1016/j.matlet.2005.03.037.
- [23] J.C. Bulmahn, G. Tikhonowski, A.A. Popov, A. Kuzmin, S.M. Klimentov, A.V. Kabashin, P.N. Prasad, Laser-ablative synthesis of stable aqueous solutions of elemental bismuth nanoparticles for multimodal theranostic applications, Nanomaterials 10 (8) (2020) http://dx.doi.org/10.3390/nano10081463.
- [24] S. Dadashi, H. Delavari, R. Poursalehi, Optical properties and colloidal stability mechanism of bismuth nanoparticles prepared by Q-switched Nd:YAG laser ablation in liquid, Procedia Mater. Sci. 11 (2015) 679–683, http://dx.doi.org/ 10.1016/j.mspro.2015.11.027, 5th International Biennial Conference on Ultrafine Grained and Nanostructured Materials, UFGNSM15.
- [25] S. Dadashi, R. Poursalehi, H. Delavari H., Formation, gradual oxidation mechanism and tunable optical properties of Bi/Bi<sub>2</sub>O<sub>3</sub> nanoparticles prepared by Nd:YAG laser ablation in liquid: Dissolved oxygen as genesis of tractable oxidation, Mater. Res. Bull. 97 (2018) 421–427, http://dx.doi.org/10.1016/j.materresbull.2017.09.029.
- [26] S. Dadashi, R. Poursalehi, H. Delavari, Optical and structural properties of Bibased nanoparticles prepared via pulsed Nd:YAG laser ablation in organic liquids, Appl. Phys. A 124 (6) (2018) 406, http://dx.doi.org/10.1007/s00339-018-1817-
- [27] M. Elabbasy, M. Abd El-Kader, A. Ismail, A. Menazea, Regulating the function of bismuth (III) oxide nanoparticles scattered in Chitosan/Poly (Vinyl Pyrrolidone) by laser ablation on electrical conductivity characterization and antimicrobial activity, J. Mater. Res. Technol. 10 (2021) 1348–1354, http://dx.doi.org/10. 1016/j.jmrt.2020.12.109.
- [28] L. Escobar-Alarcón, E. Velarde Granados, D. Villa Sanchez, O. Olea-Mejia, E. Haro-Poniatowski, A. Arrieta Castañeda, D.A. Solis-Casados, Bismuth and gold nanoparticles prepared by laser ablation in aqueous solutions, in: Science and Materials Engineering IV, in: Advanced Materials Research, vol. 976, Trans Tech Publications Ltd, 2014, pp. 196–201, http://dx.doi.org/10.4028/www.scientific.net/AMR.976.196.
- [29] M. Flores-Castañeda, S. Camacho-Lopez, Si nanoparticle decorated Bi<sub>2</sub>O<sub>2</sub>CO<sub>3</sub> 2D nanocomposite synthesized by femtosecond laser ablation of solids in liquids and aging, Opt. Laser Technol. 158 (2023) 108891, http://dx.doi.org/10.1016/j.optlastec.2022.108891.
- [30] M.F. Castañeda, S. Camacho-López, V.H. Castrejón-Sánchez, C.B. Morales-Ramos, M. Camacho-López, Study of the oxidation process of bismuth nanoparticles using NaClO, Nanotechnology 34 (20) (2023) 205706, http://dx.doi.org/10. 1088/1361-6528/acb445.

- [31] L.D. Geoffrion, D. Medina-Cruz, M. Kusper, S. Elsaidi, F. Watanabe, P. Parajuli, A. Ponce, T.B. Hoang, T. Brintlinger, T.J. Webster, G. Guisbiers, Bi<sub>2</sub>O<sub>3</sub> nano-flakes as a cost-effective antibacterial agent, Nanoscale Adv. 3 (2021) 4106–4118, http://dx.doi.org/10.1039/D0NA00910E.
- [32] M.A. Gondal, T.A. Saleh, Q. Drmosh, Optical properties of bismuth oxide nanoparticles synthesized by pulsed laser ablation in liquids, Sci. Adv. Mater. 4 (3–4) (2012) 507–510, http://dx.doi.org/10.1166/sam.2012.1310.
- [33] R.A. Ismail, F.A. Fadhil, Effect of electric field on the properties of bismuth oxide nanoparticles prepared by laser ablation in water, J. Mater. Sci., Mater. Electron. 25 (3) (2014) 1435–1440, http://dx.doi.org/10.1007/s10854-014-1747-z.
- [34] R.I. Kamel, D.S. Ahmed, U.M. Nayef, Synthesis of Bi<sub>2</sub>O<sub>3</sub> nanoparticles by laser ablation on porous silicon for photoconversion application, Optik 193 (2019) 163013, http://dx.doi.org/10.1016/ji.ijleo.2019.163013.
- [35] C.B. Morales-Ramos, M. Camacho-López, M.A. Camacho-López, A.R. Vilchis-Nestor, M. Flores-Castañeda, S. Camacho-López, ô-Bi2O3 nanoparticles obtained by laser ablation of solids in liquids, Mater. Lett. 309 (2022) 131415, http://dx.doi.org/10.1016/j.matlet.2021.131415.
- [36] S.S. Shaker, R.A. Ismail, D.S. Ahmed, Preparation of bismuth oxide nanoplatelets/Si photodetector by laser ablation in liquid under effect of an external magnetic field, Silicon 14 (1) (2022) 107–113, http://dx.doi.org/10. 1007/s12633-020-00789-4.
- [37] L. Torrisi, N. Restuccia, L. Silipigni, S. Cuzzocrea, M. Cordaro, Synthesis of bismuth nanoparticles for biomedical applications, Atti Accad. Pelorit. Pericolanti - Cl. Sci. Fis. Mat. Natur. 97 (S2) (2019) 12, http://dx.doi.org/10.1478/AAPP. 97S2A12.
- [38] L. Torrisi, L. Silipigni, N. Restuccia, S. Cuzzocrea, M. Cutroneo, F. Barreca, B. Fazio, G. Di Marco, S. Guglielmino, Laser-generated bismuth nanoparticles for applications in imaging and radiotherapy, J. Phys. Chem. Solids 119 (2018) 62–70, http://dx.doi.org/10.1016/j.jpcs.2018.03.034.
- [39] R. Karimzadeh, J.Z. Anvari, N. Mansour, Nanosecond pulsed laser ablation of silicon in liquids, Appl. Phys. A 94 (4) (2009) 949–955, http://dx.doi.org/10. 1007/s00339-008-4873-8.
- [40] R. Fabbro, J. Fournier, P. Ballard, D. Devaux, J. Virmont, Physical study of laser-produced plasma in confined geometry, J. Appl. Phys. 68 (2) (1990) 775–784, http://dx.doi.org/10.1063/1.346783, arXiv:https://pubs.aip.org/aip/jap/article-pdf/68/2/775/7467613/775\_1\_online.pdf.
- [41] A. Salazar-Pérez, M. Camacho-López, R. Morales-Luckie, V. Sánchez-Mendieta, F. Ureña-Núñez, J. Arenas-Alatorre, Structural evolution of Bi<sub>2</sub>O<sub>3</sub> prepared by thermal oxidation of bismuth nano-particles, Superf. Vacío 18 (3) (2005) 4–8.
- [42] A. Dutta, I. Zelocualtecatl Montiel, K. Kiran, A. Rieder, V. Grozovski, L. Gut, P. Broekmann, A tandem (Bi<sub>2</sub>O<sub>3</sub> → Bi<sub>m</sub>et) catalyst for highly efficient ec-CO<sub>2</sub> conversion into formate: Operando Raman spectroscopic evidence for a reaction pathway change, ACS Catal. 11 (9) (2021) 4988–5003, http://dx.doi.org/10.1021/acscatal.0c05317, arXiv:https://doi.org/10.1021/acscatal.0c05317.

- [43] Y. Astuti, B. Listyani, L. Suyati, A. Darmawan, Bismuth oxide prepared by sol-gel method: Variation of physicochemical characteristics and photocatalytic activity due to difference in calcination temperature, Indones. J. Chem. 21 (1) (2020) 108–117, http://dx.doi.org/10.22146/ijc.53144.
- [44] M. Selvapandiyan, K. Sathiyaraj, Synthesis, preparation, structural, optical, morphological and elemental analysis of bismuth oxides nanoparticles, Silicon 12 (10) (2020) 2309–2315, http://dx.doi.org/10.1007/s12633-019-00327-x.
- [45] Y. Zhang, Q. Shao, C. Chen, H. Jiang, F. Su, Q. Hu, Z. Guo, Microwave-hydrothermal synthesis of beta-bismuth (III) oxide nanopowders and their enhanced photocatalytic properties, Powder Technol. 370 (2020) 226–236, http://dx.doi.org/10.1016/j.powtec.2020.05.068.
- [46] L. Álvarez, B. Rojas de Gascue, R.J. Tremont, E. Márquez, E.J. Velazco, Synthesis and characterization of a new aluminum-doped bismuth subcarbonate, Crystals 9 (9) (2019) http://dx.doi.org/10.3390/cryst9090466.
- [47] F. He, Z. He, J. Xie, Y. Li, IR and Raman spectra properties of Bi<sub>2</sub>O<sub>3</sub>-ZnO-B<sub>2</sub>O<sub>3</sub>-BaO quaternary glass system, Am. J. Anal. Chem. 5 (16) (2014) 9, http://dx.doi.org/10.4236/ajac.2014.516121.
- [48] Z.A. Zulkifli, K.A. Razak, W.N.W.A. Rahman, The effect of reaction temperature on the particle size of bismuth oxide nanoparticles synthesized via hydrothermal method, AIP Conf. Proc. 1958 (1) (2018) 020007, http://dx.doi.org/10. 1063/1.5034538, arXiv:https://pubs.aip.org/aip/acp/article-pdf/doi/10.1063/1. 5034538/14157104/020007\_1\_online.pdf.
- [49] K. Valencia G., A. López, A. Hernández-Gordillo, R. Zanella, S.E. Rodil, Stabilized β-Bi2O3 nanoparticles from (BiO)<sub>4</sub>CO<sub>3</sub>(OH)<sub>2</sub> precursor and their photocatalytic properties under blue light, Ceram. Int. 44 (18) (2018) 22329–22338, http://dx.doi.org/10.1016/j.ceramint.2018.08.358.
- [50] A. Reshak, Z. Alahmed, S. Auluck, A density functional study of the electronic properties of bismuth subcarbonate Bi2O2CO3, Solid State Sci. 38 (2014) 138–142, http://dx.doi.org/10.1016/j.solidstatesciences.2014.10.012.
- [51] C.-H. Ho, C.-H. Chan, Y.-S. Huang, L.-C. Tien, L.-C. Chao, The study of optical band edge property of bismuth oxide nanowires α-Bi2O3, Opt. Express 21 (10) (2013) 11965–11972, http://dx.doi.org/10.1364/OE.21.011965.
- [52] H. Huang, N. Tian, S. Jin, Y. Zhang, S. Wang, Syntheses, characterization and nonlinear optical properties of a bismuth subcarbonate Bi<sub>2</sub>O<sub>2</sub>CO<sub>3</sub>, Solid State Sci. 30 (2014) 1–5, http://dx.doi.org/10.1016/j.solidstatesciences.2014.01.010.
- [53] I.Y. Khairani, G. Mínguez-Vega, C. Doñate-Buendía, B. Gökce, Green nanoparticle synthesis at scale: a perspective on overcoming the limits of pulsed laser ablation in liquids for high-throughput production, Phys. Chem. Chem. Phys. 25 (2023) 19380–19408, http://dx.doi.org/10.1039/D3CP01214J.